Monthly Notices of the ROYAL ASTRONOMICAL SOCIETY

MNRAS **535,** 434–442 (2024) https://doi.org/10.1093/mnras/stae2402
Advance Access publication 2024 October 26

A gamma-ray stacking survey of Fermi-LAT undetected globular clusters

Owen K. Henry [1,2★] Timothy A.D. Paglione [1,2,3] Yuzhe Song (宋宇哲) [4,5] Joshua Tan [2,6] David Zurek[2] and Vanessa Pinto[7]

[1]*Department of Physics, The Graduate Center, City University of New York, 365 Fifth Ave., New York, NY 10016, USA*
[2]*Department of Astrophysics, American Museum of Natural History, Central Park West at 79th Street, New York, NY 10024, USA*
[3]*Department of Earth and Physical Sciences, York College, City University of New York, 94-20 Guy R. Brewer Blvd., Jamaica, NY 11451, USA*
[4]*Center for Astrophysics and Supercomputing, Swinburne University of Technology, John St, Hawthorn, VIC 3122, Australia*
[5]*OzGrav, ARC Center for Excellence in Gravitational Wave Discovery , Level 9 AMDC Building, Swinburne University of Technology, John St, Hawthorn VIC 3122, Australia*
[6]*Department of Natural Sciences, LaGuardia Community College, City University of New York, 31-10 Thomson Ave, Long Island City, NY 11101, USA*
[7]*Max Planck Institute for Radio Astronomy, Auf dem Hügel 69, D-53121 Bonn, Germany*

Accepted 2024 October 15. Received 2024 September 24; in original form 2024 June 13

ABSTRACT

We present evidence for γ-ray emission from a stacked population of 39 high-latitude globular clusters (GCs) not detected in the Fermi Point Source Catalogue, likely attributable to populations of millisecond pulsars within them. In this work, we use 13 yr of data collected by the Large Area Telescope aboard the *Fermi Gamma-Ray Space Telescope* to search for a cumulative signal from undetected GCs and compared them to control fields (CFs), selected to match the celestial distribution of the target clusters so as to distinguish the γ-ray signal from background emission. The joint likelihood distribution of the GCs has a significant separation ($\sim 4\sigma$) from that of the CFs. We also investigate correlations between detected cluster luminosities and other cluster properties such as distance, the number of millisecond pulsars associated with each cluster, and stellar encounter rate but find no significant relationships.

Key words: pulsars: general – globular clusters: general – gamma-rays: general.

1 INTRODUCTION

The Large Area Telescope (LAT) aboard the *Fermi Gamma-ray Space Telescope* has been measuring the most energetic phenomena in The Universe since 2008. During its mission, it has detected γ-rays from many different source classes including globular clusters (GCs). The first GC detected by the LAT was 47 Tuc (Abdo et al. 2009a), and soon after there were studies of γ-ray emission from other GCs using the LAT such as Terzan 5 (Kong, Hui & Cheng 2010), M15 (Zhang et al. 2016), M80 (Tam et al. 2011), and many others (Hooper & Linden 2016; Lloyd, Chadwick & Brown 2018; Yuan et al. 2022a, b). Today, there are a total of 32 detected GCs in the 12-yr LAT catalogue, 4FGL-DR3 (Abdollahi et al. 2022, hereafter 4FGL). GCs have proven to be an ideal environment for millisecond pulsars (MSPs) because MSPs are most likely formed through recycling processes in binary systems. Thus, the high density and encounter rate of a GC can foster efficient MSP formation (Bhattacharya & van den Heuvel 1991; Tauris & van den Heuvel 2006; D'Antona & Tailo 2020). When the neutron star's companion overflows its Roche lobe, material accretes onto the neutron star depositing angular momentum and decreasing the neutron star spin period down to the millisecond regime. Such mass-exchange binary systems appear as low-mass X-ray binaries (LMXBs) (Bhattacharya 1996) and are the prime progenitor candidates of MSPs (Alpar et al. 1982). Per unit mass, LMXBs are two orders of magnitude more abundant in GCs than in the Galactic field (Clark 1975; Katz 1975; Grindlay & Bailyn 1988). MSPs are found in excess in GCs at a similar order of magnitude. To date, over 330 MSPs have been detected in at least 44 GCs (Freire 2024).

The hypothesis that MSPs are the primary source of γ-rays from GCs is supported by detections of pulsed γ-ray emission in the millisecond regime from GCs over the mission time of Fermi (Freire et al. 2011; Johnson et al. 2013; Zhang et al. 2023). To this end, Wu et al. (2022) investigated spectral energy distributions (SEDs) of 104 MSPs detected with LAT and compared them to SEDs of detected GCs in the 4FGL. They aimed to identify contributions from two leptonic processes that are thought to govern the emission physics of γ-rays around MSPs: curvature radiation coming directly from the pulsars, and inverse-Compton (IC) scattered background photons from the CMB, the Galactic radiation field, or the dense radiation field of the cluster itself (Harding, Usov & Muslimov 2005). Wu et al. (2022) concluded that it is unclear which emission mechanism dominates.

In this study, we look for γ-ray signals from GCs yet undetected by Fermi. We also aim to leverage the low luminosity clusters examined in this study to extend correlation analyses between the γ-ray luminosity (L_γ) and various cluster properties. In addition, this correlation studies could help inform follow-up observations of clusters to search for undetected radio pulsars. In this study,

★ E-mail: ohenry@gradcenter.cuny.edu

we conduct correlation tests similar to that of de Menezes, Cafardo & Nemmen (2019), Song et al. (2021), and Feng et al. (2024) between the γ-ray luminosity (L_γ) of detected GCs and three physical properties that are related to the dynamics of the GC: the stellar encounter rate, the number of MSPs, and the photon field density.

We present this work as follows: In Section 2 the data selection criteria for the γ-ray target GCs are described and their data processing procedure from `fermipy` is discussed. In Section 3 we describe our stacking procedures. In Section 4 the data analysis and results are discussed, including stack significance and correlation analyses. In Section 5 we review and summarize our results as well as suggest possible directions forward.

2 OBSERVATIONS

2.1 Target selection

We select our set of target GCs from Harris (2010) with a Galactic latitude cut of $|b| > 20^\circ$ to avoid the complex background of the γ-ray bright plane of the Galaxy and excluding clusters that are already detected in the 4FGL. These selection criteria yield 39 target GCs.

For comparison, we select control fields (CFs) by generating a randomly distributed sample matching the Galactic latitude and longitude distributions of the target GCs, and $|b| > 20^\circ$. To avoid contamination, we excluded CFs centred within 1.7°, a distance of roughly twice the containment radius of our targets or 4FGL sources. In the end, we use 90 CFs for the analysis. With roughly double the CF test sources as target GCs, we sufficiently capture the Poisson variance while minimizing computational expense. This procedure for selecting CFs is standard practice (e.g. Paliya et al. 2019; Di Mauro et al. 2023; McDaniel et al. 2024). The locations of all target sources, control fields, and 4FGL-detected clusters are shown in Fig. 1. We test the validity of this population selection of CF test sources in Section 4.1.

2.2 Binned likelihood analysis

We adopt a typical maximum-likelihood analysis to search for γ-ray emission from our targets (Mattox et al. 1996). Thirteen years of LAT data between mission elapsed time (MET) 239 160 000 s and 651 715 205 s were used in this study. We filtered data using a zenith angle cut of 90° to avoid contamination from the Earth. The photon energy range for analysis is 300 MeV to 100 GeV, which is split into 30-logarithmically spaced bins.[1] This energy range has been shown to maximize the sensitivity of the analysis (Paliya et al. 2020; Song et al. 2023). All-sky livetime and exposure cubes were created for all 129 (39 targets plus 90 CF) regions of interest (ROIs) that we consider in this analysis. We use the third revision of the Pass 8 (P8R3) instrument response function (P8R3_SOURCE_V3), the most recent Galactic emission model (`gll_iem_v07.fits`), and isotropic background emission model (`iso_P8R3_SOURCE_V3_v1.txt`) (Abdo et al. 2009b) with the default event class and type (evclass = 128, evtype = 3).[2]

We perform this analysis using `fermipy`, a Python package that facilitates analysis of LAT data with the Fermi Science Tools within the open source distribution of Python, ANACONDA (Wood et al. 2017; Fermi Science Support Development Team 2019; Anaconda 2020). We perform the maximum-likelihood test for the presence of a γ-ray point source at each target's location on the sky. The result of the likelihood analysis is the Test Statistic (TS), defined as $\mathrm{TS} = 2\ln(L/L_0)$, where L is the likelihood of a point source being present at the centre of the ROI, and L_0 is the null hypothesis that there is no central source (Mattox et al. 1996). The detection significance can be estimated from $\sqrt{\mathrm{TS}}$, and we adopt the usual detection threshold of $\mathrm{TS} > 25$ (Abdollahi et al. 2022).

The ROIs are $21^\circ \times 21^\circ$ square cutouts on the sky centred around each target coordinate. We model an additional point source at the centre of the ROI with a spectral model that is described below in Section 2.3. Spectral parameters of 4FGL sources within 5° of the centre of the ROI are free to be fit, and those outside remain fixed. The spectral model adopted in this study is discussed in the following section (Section 2.3).

We search for additional unmodelled point sources by generating TS maps for each ROI using `gta.find_sources`. We search for power-law sources with a spectral index of -2 outside of a 0.3° radius from the ROI centre and then identify sources with a minimum detection threshold of $\mathrm{TS} > 25$. Sources that peak above this threshold have their spectral parameters fit and are then added to the model. TS values for all target GCs in this study are presented in Table 1. We conduct an identical analysis for the CF test sources.

2.3 Spectral modelling of globular clusters

We test two different spectral models to maximize the sensitivity of our analysis. The spectral models most commonly used for GCs are `LogParabola` (LP) and `PowerLawSuperExpCutoff` (PLEC).[3] The Fermi LAT consortium typically uses the LP spectral model to fit GCs, but several studies fit GC spectra with the PLEC model (Bednarek & Sitarek 2007; Lloyd et al. 2018; de Menezes et al. 2019). The spectral flux given by the PLEC model is

$$\frac{\mathrm{d}N}{\mathrm{d}E} = N_0 \left(\frac{E}{E_0}\right)^{\gamma} e^{-(E/E_c)^b}, \tag{1}$$

where N_0 is the normalization pre-factor, γ is the power-law spectral index, E_0 is the energy scale factor, E_c is the cutoff energy, and b is a second power-law index that determines the curvature at the cutoff. We also test the LP model:

$$\frac{\mathrm{d}N}{\mathrm{d}E} = N_0 \left(\frac{E}{E_0}\right)^{-(\gamma+\beta\log(E/E_0))}, \tag{2}$$

where β measures the spectral curvature (Massaro et al. 2006). Again E_0 is a fixed scale parameter, γ is the spectral index, and N_0 is the normalization. We find no significant difference in TS when modelling the 4FGL GCs with the PLEC model compared to that of an LP model. So, we adopt the PLEC spectral model fits for all subsequent analyses and discussions in this work. The principal advantage of using the PLEC model is that it has fewer degrees of freedom, tending to yield a higher significance for a given TS. The cutoff energy (E_c) and the energy scale (E_0) were fixed at 1000 MeV. The second power-law index was also fixed at $b = 1$ (for justification, see Song et al. 2023). Only the spectral index and normalization pre-factor is free to fit.

[1] Fermi science tools and fermipy tutorials: https: //fermi.gsfc.nasa.gov/ssc/data/analysis/scitools/ and http://fermipy.readthedocs.io/en/latest/quickstart.html.

[2] https://fermi.gsfc.nasa.gov/ssc/data/access/lat/BackgroundModels.html

[3] https://fermi.gsfc.nasa.gov/ssc/data/analysis/scitools/source_models.html

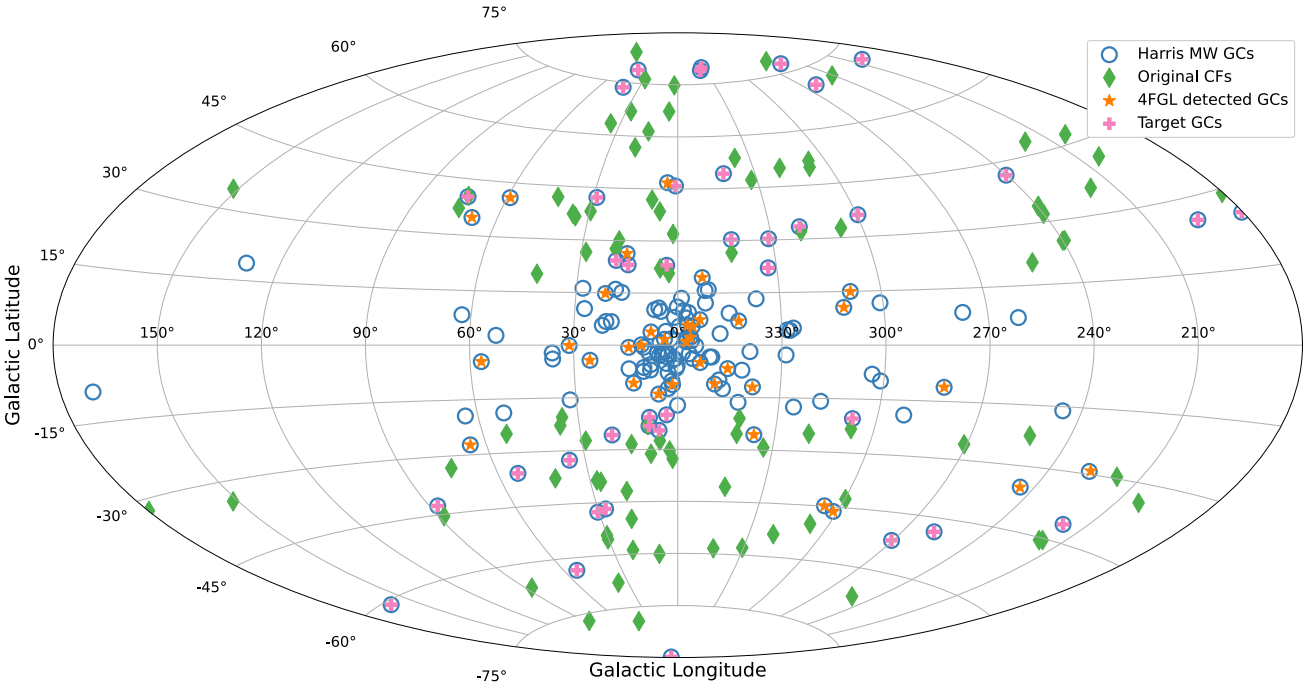

Figure 1. All-sky map of the target clusters analysed in this work (crosses), the detected GCs in the 4FGL (stars), and the control field test sources (diamonds).

Table 1. Maximum-likelihood results for target globular clusters.

Name	RA (°)	Decl (°)	TS	Name	RA (°)	Decl (°)	TS
NGC 288	13.198	−26.590	< 0.1	Whiting	30.506	−3.248	0.711
NGC 1261	48.064	−55.217	< 0.1	AM1	58.761	−49.614	3.032
Eridanus	66.185	−21.187	0.277	NGC 2419	114.535	38.882	< 0.1
Ko 2	119.567	26.246	< 0.1	Pal 3	151.381	0.071	1.623
Pal 4	172.320	28.973	1.246	Ko 1	179.828	12.253	< 0.1
NGC 4147	182.526	18.542	1.033	NGC 4590	189.860	−26.742	< 0.1
NGC 5024	198.230	18.169	4.811	NGC 5053	199.112	17.698	8.682
NGC 5272	205.546	28.375	7.699	AM4	208.958	−27.173	2.180
NGC 5466	211.363	28.534	0.123	NGC 5634	217.405	−5.976	< 0.1
NGC 5694	219.902	−26.538	7.519	IC 4499	225.077	−82.213	17.626
NGC 5824	225.993	−33.067	< 0.1	Pal 5	229.022	−0.108	4.272
NGC 5897	229.352	−21.010	0.601	Pal 14	242.770	14.958	1.456
NGC 6171	248.133	−13.053	< 0.1	NGC 6229	251.745	47.527	2.366
NGC 6254	254.287	−4.099	5.802	Pal 15	255.010	0.542	0.772
Terzan 7	289.432	−34.657	< 0.1	Arp2	292.191	−30.353	11.056
NGC 6809	294.997	−30.962	10.954	Terzan 8	295.437	−34.0002	6.740
NGC 6864	301.520	−21.921	1.025	NGC 6981	313.366	−12.537	< 0.1
NGC 7089	323.372	−0.005	0.031	NGC 7099	325.091	−23.179	17.409
Pal 12	326.661	−21.251	9.426	Pal 13	346.685	12.772	0.635
NGC 7492	347.111	−15.611	13.59				

3 RESULTS

3.1 Cumulative TS distributions

The target GCs and CFs are stacked following the procedure developed by Song et al. (2023), which was adapted from the technique of Huber et al. (2012). Fig. 2 shows the TS distributions of the central sources in the target and CF ROIs. The $\chi^2/2$ distribution, corresponding to the theoretical null (Wilks 1938), is also shown for comparison. We sum the TS values of the 39 target GCs and compare the result to an equivalent cumulative TS distribution for the CF test sources (Fig. 2). For the CF test source sum, we randomly draw 39 of the 90 fields 100 times and calculate the average sum of the cumulative TS values as a function of the stacked number of ROIs. The stack of the target clusters is displayed with 1000 random reorderings of the sum to illustrate its variation. There is a separation of $\Delta\mathrm{TS} = 59$ between the target GC and CF test source populations. We quantify the separation significance in Section 4.1. Finally, both the target GC and CF test source stacks diverge significantly from the theoretical null (which also stacks to a non-zero cumulative TS) indicating the signal in both the sample and the blank sky.

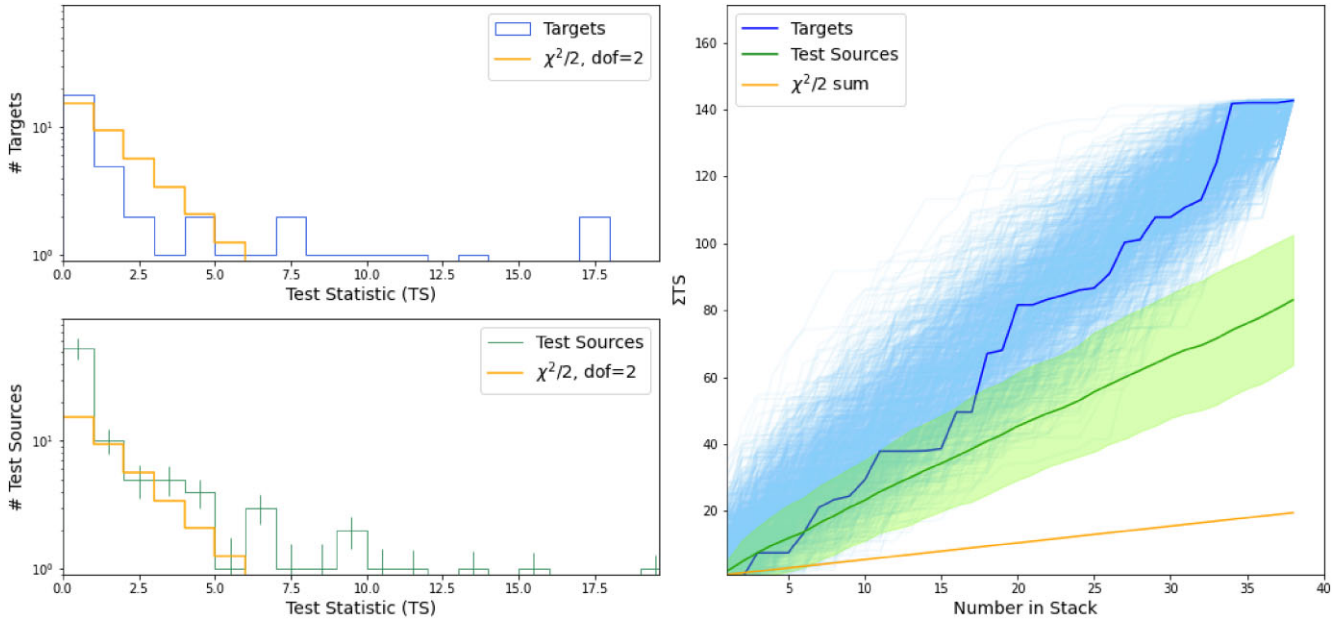

Figure 2. (Left) Histograms of the TS values of target GCs (top) and CF test sources (bottom). The CF test source histogram and error bars are the average and standard deviation of randomly selecting 39 of the 90 sources 100 times. The theoretical null ($\chi^2/2$) is shown for comparison. (Right) Cumulative TS of the GCs compared to CF test sources. The target TS stack is a randomly ordered sum of all measured TS values (Table 1). The webbed envelope shows 1000 iterations of the sum done in different random orders. The CF test source stack is the sum of 39 randomly sampled fields out of the 90 CF test sources; the lower line and shaded envelope depict the mean sum and standard deviation, respectively, as a function of stacked ROIs. The sum of the theoretical null is also shown.

3.2 Parameter space stacking analysis

The target GCs and CF test sources undergo another TS stacking procedure by fitting their spectral properties similar to Paliya et al. (2019).

As described in Section 2.2, a point source with a PLEC spectrum is placed at the coordinates of the target GC. In this fit, however, only the normalization of the Galactic and diffuse background models are free to fit. We compute the log-likelihood for the ROI for a fixed spectral index and flux and repeat this process over a grid of γ and flux values. To convert this log-likelihood map into a TS map, we adopt a null likelihood (L_0) at the lowest flux and index coordinate of the parameter space, subtract it from the rest of the map, and multiply by 2. The TS maps of each target GC are stacked to construct a parameter space significance map for our undetected cluster population. We take a resampled average of the CF test sources shown in the right panel of Fig. 3. A separation between the target GCs and CF test sources is again evident (ΔTS $= 47$) between the peak TS of the targets and the controls. For the target GCs, the significance peaks at $\gamma = -2.7^{+0.8}_{-1.5}$ and $\log(\text{flux}) = -9.2^{+0.2}_{-1.3}$ (ph cm^{-2} s^{-1}).

Two of the sources in our target GC population have a TS > 16: NGC 7099 (M 30) and IC 4499. We discuss these sources in Appendix A. Even after removing these two sources from the cumulative TS and parameter space stacking analyses, the target GC population is still more significant than the CF test sources, which we quantify in Section 4.1.

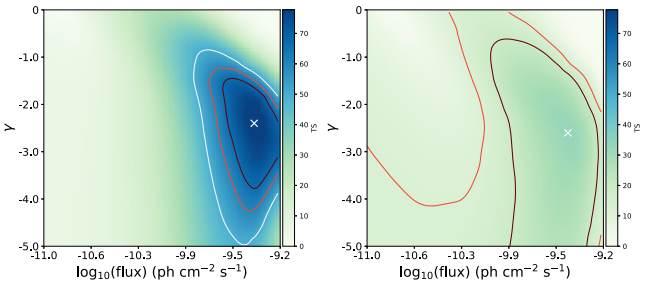

Figure 3. (Left) PLEC model parameter stack for the target GCs. The parameter stack peaks at a spectral index of $-2.3^{+0.9}_{-1.5}$, log(flux) of $-9.2^{+0.2}_{-1.3}$ ph cm^{-2}s^{-1}, and TS $= 79$. (Right) CF test sources PLEC fit parameter stack with maximum TS $= 32$. The contours represent the 3, 4, and 5σ distances from the best-fitting location in the map. This map was created by again sampling 39 out of the 90 CF test sources 1000 times and then averaging over the 1000 random samplings. The colour scale is set to the peak value of the target GC parameter space map.

4 DISCUSSION

4.1 Stack detection significance

To robustly quantify the separation between our target GC and CF cumulative TS (Fig. 2), and thus establish a stack detection, we model the γ-ray photon counts from a sub-threshold population. The model assumes that the photon counts per pixel follow a Poisson distribution, the high latitude γ-ray background is isotropic, and the spatial distribution of source counts is a 2D Gaussian with a full width at half-maximum (FWHM) of 0.5°. We assume a source population that follows a power-law distribution with flux, $N \propto S^{-\alpha}$, where N is the number of sources per bin, S is the photon flux, and α is the power-law index. The normalization depends on the signal-to-noise ratio (SNR). Here the SNR compares the total counts on source (source plus background) to the total background counts in the same number of pixels. The ratio of source to background counts, which we will refer to as the gain $g = \text{SNR} - 1$, is necessarily well below unity for a sub-threshold source. Our objective is to

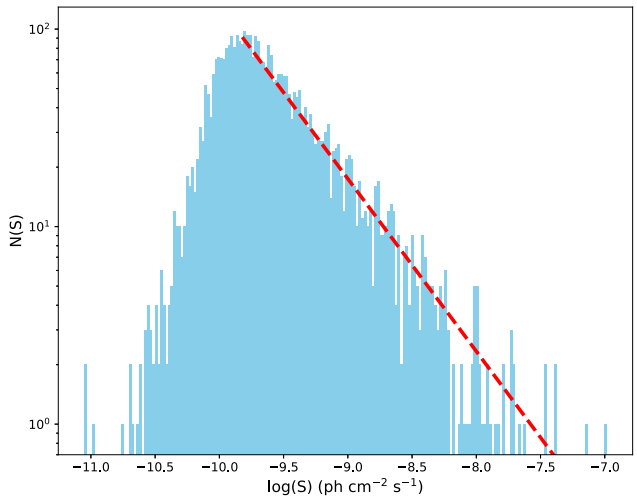

Figure 4. Histogram of high latitude 4FGL source fluxes. The linear fit (dashed line) has a slope of $\alpha = -0.873$. The plotted fluxes are the `flux1000` measurements from the 4FGL-DR3 catalogue (`gll_psc_v28.fit`).

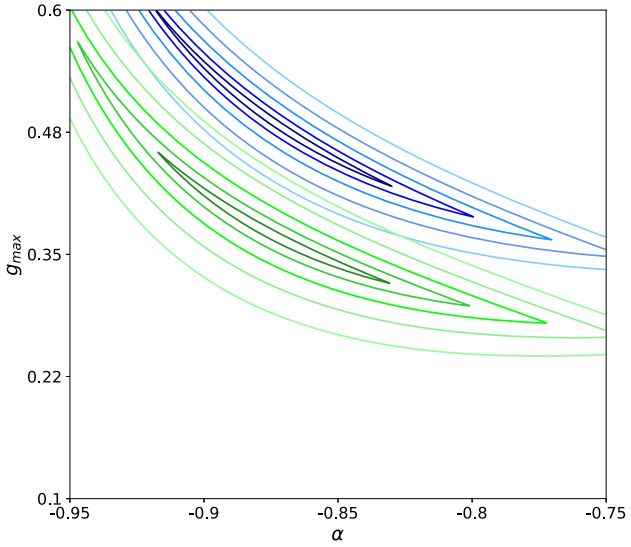

Figure 5. Significance maps ($\sqrt{\Delta TS}$) characterizing the source populations underlying the GC (above) and CF (below) stacks. The contours are 1, 2, 3, 4, and 5σ away from each global minimum.

reproduce the observed cumulative TS values of the target GCs and CF test sources using a distribution of model point sources with varied g and a power-law index of α. We create a set of models given the slope of the distribution (α) and the size of the domain $0 < g < g_{\rm max}$, where $g_{\rm max}$ corresponds to the maximum gain of the power-law distribution as defined by the `scale` keyword argument in `scipy.stats.powerlaw.rvs`.

We explore $-0.95 \leq \alpha \leq -0.75$, which is centred on a fit of the source count of high latitude 4FGL sources (Fig. 4), measured to be $\alpha = -0.87 \pm 0.03$. We use $0.1 \leq g_{\rm max} \leq 0.6$, which yields cumulative TS values of the modelled stacks that encompass the observational results (Fig. 2).

For each value of $g_{\rm max}$ and α, a model population of 10 000 sources is synthesized by building a distribution of g values. For each model source, the gain g and the background counts are used to calculate the TS value (Mattox et al. 1996). We adopt an estimate of 20 background counts per 0.1° pixel. From these 10 000 model sources, we randomly draw 39 to match the number of our target GCs. Their TS values are summed, returning a model cumulative TS. This model stacking is done 1000 times for a given $g_{\rm max}$ and α and then averaged. Finally, we calculate the absolute value of the difference between the model results and the cumulative TS values of the target GCs and CFs (the maximum values of the distributions shown in the right panel of Fig. 2, or 144 and 85, respectively). The final target GC and CF significance distributions, $\sqrt{|\Delta TS|}$, are shown in Fig. 5. We use the Kullback–Leibler divergence (Kullback & Leibler 1951) implemented in SCIPY with `scipy.special.kl_div` to estimate the significance of the difference between these two distributions. According to that approach, the target GC stack is detected with a significance of 4.7σ over the controls. Excluding NGC 7099 and IC 4499 reduces this significance to 3.5σ, still indicating an excess signal from the target population over the controls.

Given the sparseness of our GC target population, we test the appropriateness of our CFs by probing whether our target GCs are biased towards regions of excess or anomalous γ-ray background. We generate a new CF test source population consisting of 78 ROIs with centres ±5° in Galactic longitude from each of our targets, again avoiding 4FGL sources. While we expect these test CFs to be biased due to a systematic contamination by the sub-threshold targets, it still may serve as a valuable test given the patchy and latitude-dependent structure of the LAT sensitivity (Smith et al. 2023, hereafter 3PC). The latitude distributions of our targets, these CFs, and the original CFs are statistically indistinguishable. The 3PC LAT sensitivity distributions at their locations are also statistically equivalent.

Comparing the stack of these CFs to the target stack still yields a detection significance of 3.7σ. As anticipated, the cumulative TS value of the latitude-matched CF test sources is greater than the original CF test source population by 3.4σ. While the original CFs are likely therefore more appropriate, we conservatively report a $\sim 4\sigma$ stack detection of the GC population in this study.

4.2 Correlation analysis

We investigate possible correlations between the γ-ray luminosity (L_γ) and physical cluster parameters likely to be associated with the high energy emission from GCs, namely the number of MSPs ($N_{\rm MSP}$) and stellar encounter rate (Γ). From Bahramian et al. (2013) Γ is taken to be:

$$\Gamma = A \frac{4\pi}{\sigma_c} \int \rho(r)^2 r^2 {\rm d}r, \tag{3}$$

where σ_c is the velocity dispersion at the core radius, and $\rho(r)$ is the stellar density profile of the cluster. The line-of-sight integration is performed out to the half-light radius. As defined, Γ is an index that measures the average rate of encounters within a GC. The constant A is such that Γ is normalized to 1000 encounters in the cluster 47 Tucanae (Bahramian et al. 2013). LMXBs, thought to be the progenitors of MSPs, are overabundant in GCs due to the formation of these systems through stellar interactions. It follows that for GCs, Γ could be a tracer of MSPs and thus γ-rays.

In the left panel of Fig. 6 we plot L_γ against $N_{\rm MSP}$ of the detected GCs in the 4FGL with tabulated values of $N_{\rm MSP}$ from Freire (2024).

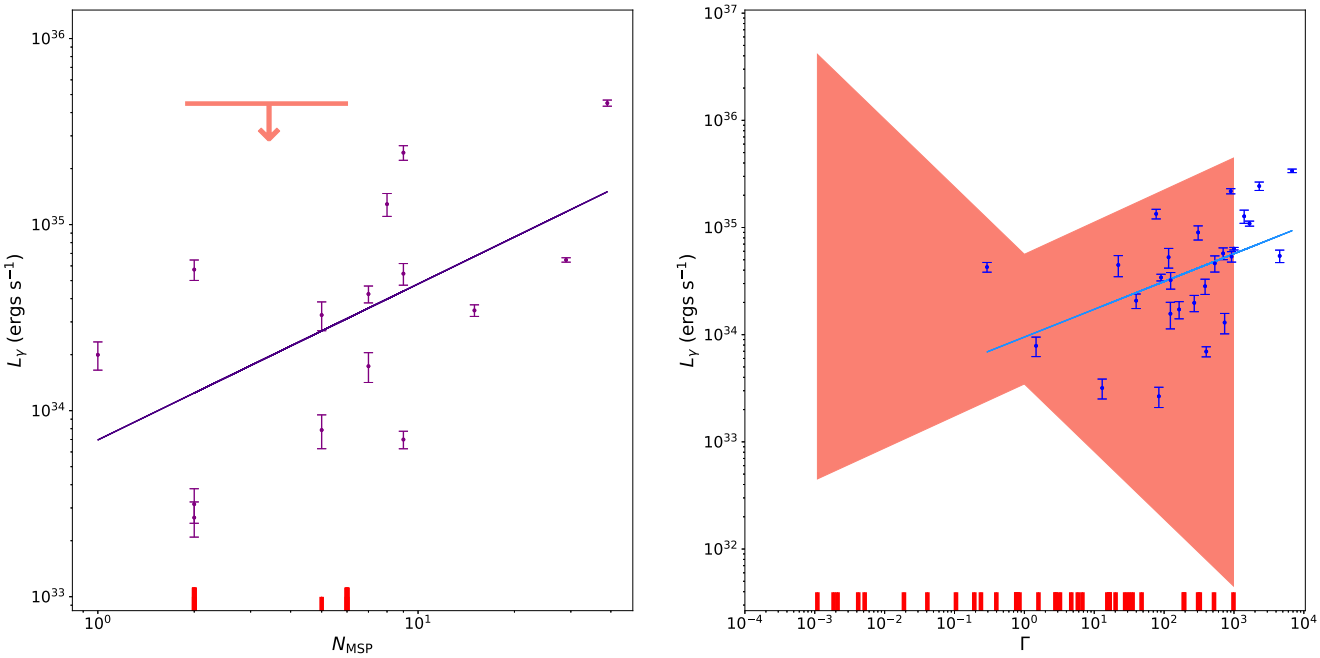

Figure 6. Correlation relations between L_γ and $N_{\rm MSP}$ (left) and Γ (right) for 4FGL GCs (dots). The vertical lines on the x-axis represent the values of undetected target GCs. (Left) L_γ versus $N_{\rm MSP}$: The values of $N_{\rm MSP}$ for the five GCs in our target population are taken from Freire (2024). Taller ticks indicate two GCs with that number of MSPs. The upper limit spans the tick marks on the x-axis. Its height is determined from the 5σ contour in Fig. 3. The data points are plotted with $N_{\rm MSP}$ from Freire (2024) and L_γ is computed using the γ-ray energy flux tabulated in the 4FGL and the cluster's distance from Harris (2010). (Right) L_γ versus Γ: The error region is centred on the mean Γ of the target GCs (equation 4). The error region is discussed in Section 4.2. The data points are plotted using Γ from Bahramian et al. (2013), and similarly L_γ is calculated from the energy flux in 4FGL and the cluster distance from Harris (2010).

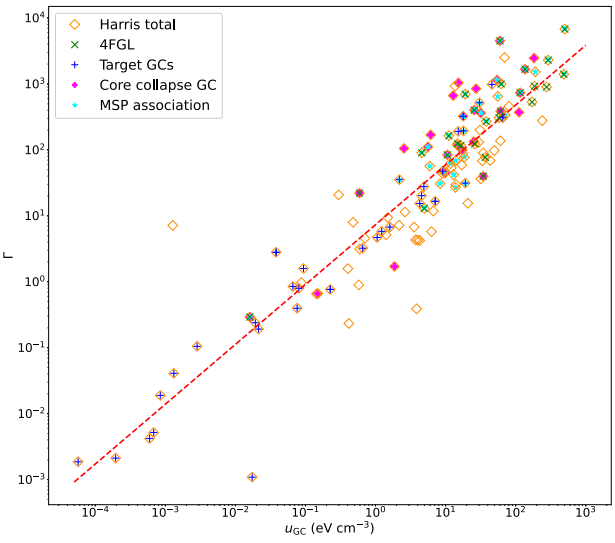

Figure 7. Encounter rate (Γ) versus cluster photon field density ($u_{\rm GC}$). Also plotted are different kinds of GCs, such as whether the cluster is core-collapsed, is known to host MSPs, or is in the 4FGL catalogue. The dotted line is the trend from a linear regression (equation 5).

The linear regression of $\log(L_\gamma)$ and $\log(N_{\rm MSP})$ for the detected 4FGL GCs returns a coefficient of determination of $R^2 = 0.37$ indicating a weak correlation between the parameters. No upper limits were used in computing this regression. Overlaid on this plot of detected 4FGL GCs we estimate the L_γ upper limit of our stacked target GC population by integrating the spectra within the 5σ contour in Fig. 3. The maximum energy flux is scaled by $4\pi d^2$, where $d = 31.8$ kpc is the median distance of our targets. This calculation provides the upper limit in the left panel of Fig. 6.

In the right panel of Fig. 6, we also perform a linear regression between L_γ and Γ of detected 4FGL GCs that have a tabulated Γ from Bahramian et al. (2013). This fit between L_γ and Γ returns a coefficient of determination of $R^2 = 0.20$, also indicating a weak correlation. Once again no upper limits were used in computing this regression. For the undetected target GCs, we test for correlation using a technique described in Khatiya et al. (2023) since there are far more target GCs with tabulated Γ (34) than there are with $N_{\rm MSP}$ (5). We assume a correlation between L_γ and Γ in the following form:

$$\log L_\gamma = a + b \log \Gamma \tag{4}$$

and then explore a grid of slopes ($-2 \leq b \leq 2$) and intercepts ($20 \leq a \leq 40$) for each target GC.

Each L_γ is then converted into an energy flux and compared to that individual target's parameter space stack result (Fig. 3, described in Section 3.2) to determine the TS (and thus the likelihood) of that luminosity. From this, we determine the most likely relationship between L_γ and Γ along with the error region shown in Fig. 6 for our target GCs. Our result is consistent with a lack of correlation and also matches the weak correlation between the detected between L_γ and Γ with a measured power-law index of $b = -0.26^{+0.56}_{-0.77}$.

We test the correlation between Γ and the photon field density of the cluster, $u_{\rm GC}$, of every GC in Harris (2010) similar to the 'hidden correlation' analysis done by Song et al. (2021) (Fig. 7). The total photon field density has two components: due to the Milky Way ($u_{\rm MW}$) and due to the GC itself ($u_{\rm GC}$), defined as $u_{\rm GC} = L_*/4\pi c R_h^2$

(Song et al. 2021). Here R_h is the half-light radius and the stellar luminosity, L_*, is estimated from the central luminosity density of the cluster multiplied by the surface integral of the 1D King model (King 1962) done in `AstroPy` (Astropy Collaboration 2022). The cluster parameters are taken from Harris (2010). We compute $u_{\rm MW}$ from the ultraviolet–infrared interstellar radiation field model of Popescu et al. (2011, 2017). In Fig. 7 we demonstrate the correlation between Γ and $u_{\rm GC}$. Detected GCs have both large Γ and $u_{\rm GC}$ while our targets have considerably lower values of each. Although this relationship is expected since both quantities depend on the stellar density of the cluster, it is notable that the relation holds over eight orders of magnitude with a coefficient of determination of $R^2 = 0.83$. The fitted trendline is given by

$$\log \Gamma = (0.91 \pm 0.04) \log u_{\rm GC} + (0.86 \pm 0.06). \quad (5)$$

Ultimately, we find no strong correlations between cluster properties and L_γ. Additionally, we agree with Song et al. (2021) that the strong underlying correlation between $u_{\rm GC}$ and Γ can potentially lead to spurious claims when looking for fundamental planes dependent on three or more variables.

5 CONCLUSIONS

In this work, we study γ-ray emission from 39 previously undetected high-latitude GCs using Fermi-LAT. Our cumulative stacking analyses return a stack separation of $\sim 4\sigma$ from CF test sources, which alludes to a significant population of sub-threshold GCs. We find either weak or no significant correlations between L_γ, Γ, and $N_{\rm MSP}$ across this study's test populations (target GCs or detected 4FGL GCs), but recover the strong correlation of Γ with photon field density $u_{\rm GC}$ found in Song et al. (2021).

ACKNOWLEDGEMENTS

This work was supported in part by the National Science Foundation under awards AST-1831412 and AST-2219090, by the NASA New York Space Grant Consortium (NYSG) under award # 80NSSC20M0096, and a NYSG Student Support Award to OKH. This project made use of computational systems and network services at the American Museum of Natural History supported by the National Science Foundation via Campus Cyberinfrastructure Grant Awards # 1827153 (CC∗ Networking Infrastructure: High-Performance Research Data Infrastructure at the American Museum of Natural History). This research has made use of the VizieR catalogue access tool, CDS, Strasbourg, France (DOI : 10.26093/cds/vizier). The original description of the VizieR service was published in 2000, A&AS 143, 23. The authors would also like to thank the referee of this publication for thoughtful insight into this study.

DATA AVAILABILITY

Fermi-LAT photon data are available through the Fermi-LAT data server.[4] Fermi-LAT analysis results (the output.xml or.npy files from Fermipy) of target clusters and control fields are available at doi.org/10.5281/zenodo.13948170 and doi.org/10.5281/zenodo.13952707, respectively. Post-processing analysis scripts, including the model to determine the stack divergence significance, will be shared upon request to the first author, given that a proper citation to this paper is provided in the work from those making the request.

[4]https://fermi.gsfc.nasa.gov/cgi-bin/ssc/LAT/LATDataQuery.cgi

REFERENCES

Abdo A. A. et al., 2009a, Science, 325, 845
Abdo A. A. et al., 2009b, ApJ, 703, 1249
Abdollahi S. et al., 2022, ApJ, 260, 53
Alpar M. A., Cheng A. F., Ruderman M. A., Shaham J., 1982, Nature, 300, 728
Anaconda I., 2020, Anaconda Software Distribution. Available at: https://docs.anaconda.com/
Astropy Collaboration 2022, ApJ, 935, 167
Bahramian A., Heinke C. O., Sivakoff G. R., Gladstone J. C., 2013, ApJ, 766, 136
Bednarek W., Sitarek J., 2007, MNRAS, 377, 920
Bhattacharya D., 1996, Int. Astron. Un. Colloq., 160, 547
Bhattacharya D., van den Heuvel E. P. J., 1991, Phys. Rep., 203, 1
Clark G. W., 1975, ApJ, 199, L143
D'Antona F., Tailo M., 2020, preprint (arXiv:2011.11385)
Di Mauro M., Pérez-Romero J., Sánchez-Conde M. A., Fornengo N., 2023, Phys. Rev. D, 107, 083030
Feng L., Cheng Z., Wang W., Li Z., Chen Y., 2024, Res. Astron. Astrophys., 24, 025001
Fermi Science Support Development Team 2019, Fermitools: Fermi Science Tools, Astrophysics Source Code Library, record ascl:1905.011
Freire, 2024, Pulsars in Globular Clusters. Available at: https://www3.mpifr-bonn.mpg.de/staff/pfreire/GCpsr.html
Freire P. C. C. et al., 2011, Science, 334, 1107
Grindlay J. E., Bailyn C. D., 1988, Nature, 336, 48
Harding A. K., Usov V. V., Muslimov A. G., 2005, ApJ, 622, 531
Harris W. E., 2010, preprint (arXiv:1012.3224)
Hooper D., Linden T., 2016, J. Cosmol. Astropart. Phys., 2016, 018
Huber B., Farnier C., Manalaysay A., Straumann U., Walter R., 2012, A&A, 547, A102
Johnson T. J. et al., 2013, ApJ, 778, 106
Katz J. I., 1975, Nature, 253, 698
Khatiya N. S., Boughelilba M., Karwin C. M., McDaniel A., Zhao X., Ajello M., Reimer A., Hartmann D. H., 2024, ApJ, 971, 84
King I., 1962, AJ, 67, 471
Kong A. K. H., Hui C. Y., Cheng K. S., 2010, ApJ, 712, L36
Kullback S., Leibler R. A., 1951, Ann. Math. Stat., 22, 79
Lloyd S. J., Chadwick P. M., Brown A. M., 2018, MNRAS, 480, 4782
Massaro E., Tramacere A., Perri M., Giommi P., Tosti G., 2006, A&A, 448, 861
Mattox J. R. et al., 1996, ApJ, 461, 396
McDaniel A., Ajello M., Karwin C. M., Di Mauro M., Drlica-Wagner A., Sánchez-Conde M. A., 2024, Phys. Rev. D, 109, 063024
de Menezes R., Cafardo F., Nemmen R., 2019, MNRAS, 486, 851
Paliya V. S., Domínguez A., Ajello M., Franckowiak A., Hartmann D., 2019, ApJ, 882, L3
Paliya V. S., Ajello M., Cao H. M., Giroletti M., Kaur A., Madejski G., Lott B., Hartmann D., 2020, ApJ, 897, 177
Popescu C. C., Tuffs R. J., Dopita M. A., Fischera J., Kylafis N. D., Madore B. F., 2011, A&A, 527, A109
Popescu C. C., Yang R., Tuffs R. J., Natale G., Rushton M., Aharonian F., 2017, MNRAS, 470, 2539
Smith D. A. et al., 2023, ApJ, 958, 191
Song D., Macias O., Horiuchi S., Crocker R. M., Nataf D. M., 2021, MNRAS, 507, 5161
Song Y., Paglione T. A. D., Tan J., Lee-Georgescu C., Herrera D., 2023, MNRAS, 524, 5854
Tam P. H. T., Kong A. K. H., Hui C. Y., Cheng K. S., Li C., Lu T. N., 2011, ApJ, 729, 90
Tauris T. M., van den Heuvel E. P. J., 2006, Compact stellar X-ray sources, Caimbridge Univ., New York, USA, 39, 623

Wilks S. S., 1938, Ann. Math. Stat., 9, 60
Wood M., Caputo R., Charles E., Di Mauro M., Magill J., Perkins J. S., Fermi-LAT Collaboration, 2017, Proc. Sci., 35th International Cosmic Ray Conference (ICRC2017), SISSA, Trieste, Vol. 301, PoS#824
Wu W., Wang Z., Xing Y., Zhang P., 2022, ApJ, 927, 117
Yuan M., Zheng J., Zhang P., Zhang L., 2022a, Res. Astron. Astrophys., 22, 055019
Yuan M., Ren C., Zhang P., Jiang Z., Zhang L., 2022b, Res. Astron. Astrophys., 22, 115013
Zhang P. F., Xin Y. L., Fu L., Zhou J. N., Yan J. Z., Liu Q. Z., Zhang L., 2016, MNRAS, 459, 99
Zhang P., Xing Y., Wang Z., Wu W., Chen Z., 2023, ApJ, 945,70

APPENDIX A: MARGINAL DETECTIONS OF NGC7099 AND IC4499

Two sources in our analysis had TS $>$ 16, namely NGC 7099 (M 30) and IC 4499 (Table 1). In Figs A1 and A2 we plot their TS maps from `fermipy` along with position data and tidal radius from Harris (2010). The `fermipy` localized positions and their errors are also plotted. In the case of NGC 7099, we have the location of a known MSP that is associated with the cluster (Freire 2024). Alongside these TS maps, we show the SED plotted with `fermipy` according to the spectral analysis described in Section 2.3.

We investigate these sources further by finding the peak TS in the sources' respective maps using the `localize` routine in `fermipy`. The peak localized TS is comparable to the original TS value with localized sexagesimal coordinates of $(325.281 \pm 0.150, -23.090 \pm 0.149)$ and $(225.165 \pm 0.133, -82.239 \pm 0.124)$ for NGC 7099 (M 30) and IC 4499, respectively. The original coordinates can be found in Table 1. The catalogued central cluster location, the `fermipy` localized position, and 1σ error radius all fall within the tidal radius of NGC 7099. For completeness, we also re-optimize the ROI. The combination of having a TS $>$ 16 and a pulsar detected within it makes NGC 7099 an intriguing source for follow-up with continued Fermi observations and analysis of the LAT photon data to identify any γ-ray pulsations or gather evidence for other non-thermal emission processes. In the case of IC 4499, there are no known pulsars within the cluster. IC 4499 is also a relatively low-density, low-encounter rate GC in our sample. The tidal radius, `fermipy` localized position, and error radius also agree with each other well. So, this marginally detected γ-ray emission points to a need for further radio and γ-ray follow-up observations in search of an emitting source like a pulsar.

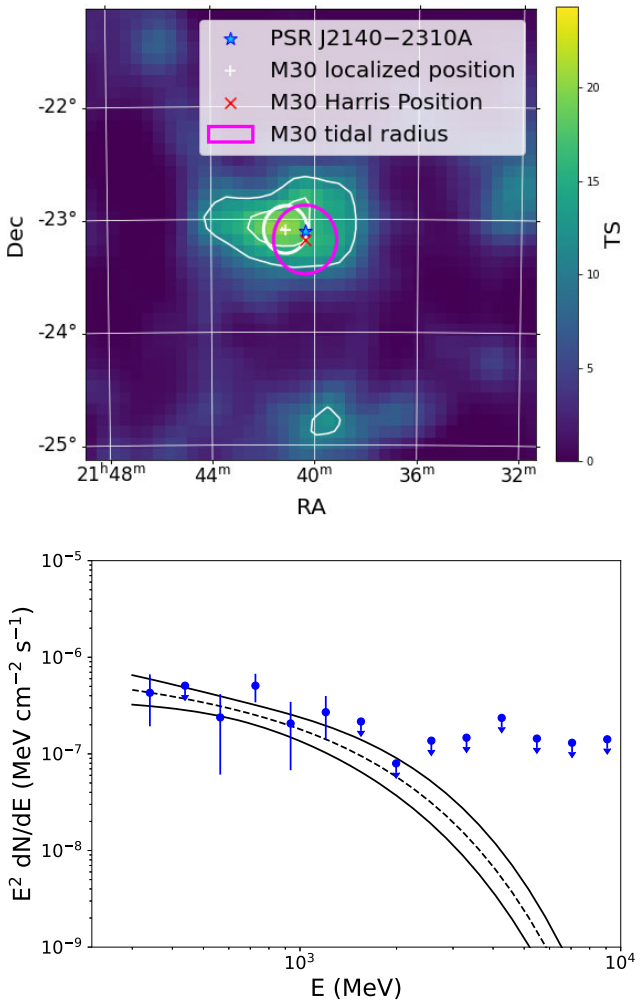

Figure A1. `fermipy` output data for NGC 7099. (Top) TS map of the central region of the ROI. The tidal radius and catalogue position are plotted from Harris (2010). The `fermipy` localized position is plotted along with its error radius according to the numbers in Appendix A. The 3σ and 5σ contours are plotted according to the model's two degrees of freedom. The position of the associated pulsar from Freire (2024) is noted by the star marker. (Bottom) `fermipy` computed spectra with a power-law index $\gamma = -2.19 \pm 0.44$ and pre-factor $N_0 = (4.8 \pm 1.6) \times 10^{-13}$ (ph cm^{-2}s^{-1}). Fluxes with error bars are shown in each energy bin with TS $>$ 4. The rest are 95 per cent CL upper limits.

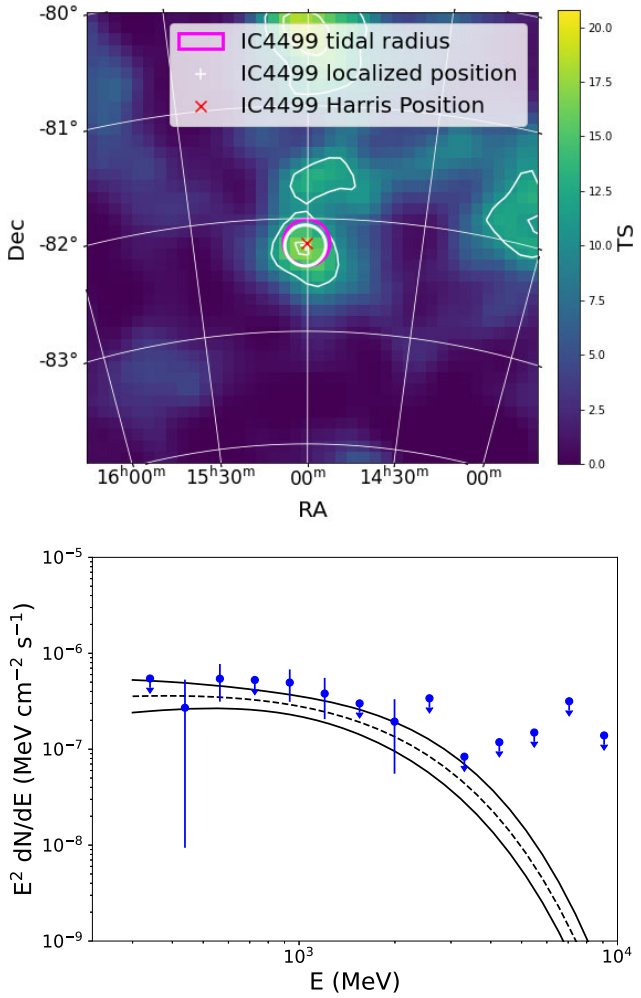

Figure A2. `fermipy` output data for IC 4499. (Top) TS map of the central region of the ROI. The tidal radius and the catalogue position are plotted from Harris (2010). The `fermipy` localized position is plotted along with its error radius according to the numbers in Appendix A. The 3σ and 5σ contours are plotted according to the model's two degrees of freedom. (Bottom) `fermipy` computed spectra with a power-law index $\gamma = -1.62 \pm 0.38$ and pre-factor $N_0 = (7.6 \pm 2.0) \times 10^{-13}$ (ph cm^{-2}s^{-1}). Fluxes with error bars are shown in each energy bin with TS > 4. The rest are 95 per cent CL upper limits.

This paper has been typeset from a TEX/LATEX file prepared by the author.